30th Symposium on Naval Hydrodynamics
Hobart, Tasmania, Australia, 2-7 November 2014

Wind-and-Wave Simulations with Dynamic Modeling for Ship Hydrodynamics Applications

Lian Shen[1,*], Shengbai Xie[2], Di Yang[3], and Yi Liu[4]
([1]University of Minnesota, [2]University of Delaware, [3]Johns Hopkins University,
[4]American Bureau of Shipping, USA)

Abstract

We develop a multiscale simulation approach for the study of wind and waves around surface-piercing structures, with an aim of computing wind loads on ships in a realistic marine atmosphere and wave environment. A far field, wind-and-wave coupled simulation is performed. An irregular, broad-banded wave field is simulated using a high-order spectral method based on potential flow theory, and a turbulent wind field is simulated using large-eddy simulation with the subgrid-scale effects dynamically modeled. The wind and wave simulations are dynamically coupled in a wave-phase resolving framework. With the inflow of wind and waves provided by the far-field simulation, a local-scale simulation around a surface-piercing object such as rectangular prism and simplified ship hull and superstructure is carried out. The air and water coupled motions are simulated using a level set method, and the presence of object is modeled using an immersed boundary method. Different aspects of the simulation are validated via a variety of tests. Our simulation results indicate that the waves have an appreciable effect on the wind loads. The method developed in this study has applications in predicting ship motions subject to wave loads together with wind loads.

1 INTRODUCTION

Besides wave loads, wind loads are another important factor that affects the operation and maneuvering of surface ships as well as cargo handling on ships. Strong wind affects the maneuverability and safety of ships (Wills, 1991; Blendermann, 2004). It has been found that the wind force on a tanker sailing with a 14m/s relative wind speed can reach up to 15% of the total drag (Matsumoto et al, 2003). Even a moderate wind can make a ship advancing at a slow speed difficult to control, and the wind force on the superstructure of a ship can be of the same order of magnitude as the wave resistance (van Berlekom, 1981). Moreover, wind can significantly contribute to the challenge of docking (Low, 1997).

Over the past several decades, numerous efforts have studied wind loads using laboratory measurement with wind tunnel tests. Valuable data have been collected for a variety of ship forms and offshore structures (see e.g. Aage et al, 1971; Blendermann, 1993; Lee and Low, 1993). The measurement data have been used by many researchers to develop statistical estimation methods for the prediction of wind loads on ships (Isherwood, 1972; Blendermann, 1993, 1994, and 1995; Haddara and Guedues Soares, 1999; Fujiwara and Nimura, 2005).

With the increase in computer power, computational fluid dynamics (CFD) has become a useful tool for the study of aerodynamics of ships and offshore structures. Most CFD studies for engineering applications use the Reynolds-averaged Navier–Stokes (RANS) formulation to take advantage of its relatively high efficiency. Different aspects of the air flow around surface ships have been studied. To name a few, Aage et al. (1997) examined wind force and smoke tracing for a ferry and an offshore platform. Yelland et al. (2002) studied air flow distortion of a research ship using CFD as well as wind tunnel test. Brizzolara and Rizzuto (2006) computed wind pres-

*Email address for correspondence: shen@umn.edu.

sure on the superstructures of large commercial ships. Wnek and Guedes Soares (2011) analyzed wind force acting on a floating LNG platform and an LNG carrier. Recently, Popinet et al. (2004) used large-eddy simulations (LES) to study the mean and turbulent characteristics of the air flow. In their LES, numerical dissipation was invoked while no explicit subgrid-scale (SGS) model was used.

In most of the above numerical studies, the wave surface was treated as a flat bottom of the computational domain of the air and the wave effect on the wind was neglected. Additionally, the inflow of wind was treated either as uniform or with a prescribed velocity profile. However, previous studies of wind–wave interactions showed that the motion and topography of the waves have strong influences on the lower part of the atmospheric boundary layer (Shemdin and Hsu, 1967; Belcher and Hunt, 1998; Sullivan et al, 2000, 2008; Yang and Shen, 2009, 2010). The wind profiles as well as wind loads are expected to depend on the wave conditions. As a result, it is desirable for the wind loads simulation study to take the interaction between wind and waves into account. Some progress has already been made in recent years towards this direction. For example, Yang et al. (2008) performed LES for the two-phase flow around a ship hull where the air–water interface was captured implicitly by a coupled level-set and volume-of-fluid method (Sussman and Puckett, 2000). Although their study focused mainly on ship hydrodynamics while the wind was less considered, it showed a promising way to study the aerodynamic problem of ships. More recently, Mousaviraad (2010) studied the effects of waves and wind on ships through numerical simulations with a semi-coupled approach of air and water: the water was not affected by air, but the air motion was computed with the free surface treated as a moving immersed boundary. The boundary layer of air was represented by a logarithmic blending function, and potential flow solutions of the waves and wind were used to impose boundary and initial conditions for air and water.

In this study, we develop a multiscale approach for the simulation of wind turbulence around surface-piercing structure in a wave field, with application to wind loads study of surface ships. To capture realistic marine atmosphere boundary layer and wave field environment in the computation, we perform coupled wind LES and wave field simulation to obtain physical inflow conditions of wind and waves for near-field simulation around the object, where LES is performed for the multiphase flow of air and water. In the near field, a level-set method is used to trace the air–water interface implicitly (Sussman et al, 1994; Osher and Fedkiw, 2001; Sethian and Smereka, 2003). The immersed boundary method (Peskin, 2002; Mittal and Iaccarino, 2005) combined with a wall-layer modeling is used to represent the surface of the object. Validations of the numerical tool developed are performed by comparison with data from literature. Using this simulation approach, we investigate the physics of the flows around a surface-piercing rectangular prism as well as a Wigley ship model. This paper is organized as follows. Section 2 introduces the numerical methods. Section 3 presents simulation results, including validations of the numerical method followed by results and discussions of canonical cases. Summary and conclusions are given in Section 4.

2 NUMERICAL APPROACH

As illustrated in Figure 1, our simulation consists of two parts. In far field, coupled simulation of wind and wave fields is performed to generate physical wind–wave inflow conditions for near-field simulation, which computes the motions of air and water around a surface-piercing object such as a surface ship or offshore structure. These two parts of simulations are introduced respectively in the two subsections below.

2.1 Simulation of wind and waves in far eld

In the far field, LES is performed for the turbulent wind field, while the wave field is simulated based on potential flow theory. The wind and wave fields are coupled dynamically at each timestep in the simulation. The numerical methods are briefly described as follows. More details can be found from Yang and Shen (2011a, b) and Yang, Meneveau, and Shen (2013a).

The motion of wind turbulence is described by the filtered single-phase Navier–Stokes equations

$$\frac{\partial \widetilde{u}_i}{\partial t} + \widetilde{u}_j \frac{\partial \widetilde{u}_i}{\partial x_j} = -\frac{1}{\rho_a}\frac{\partial \widetilde{p}}{\partial x_i} - \frac{\partial \tau^d_{ij}}{\partial x_j} - \frac{1}{\rho_a}\Pi\delta_{i1} \ , \quad (1)$$

$$\frac{\partial \widetilde{u}_i}{\partial x_i} = 0 \ . \quad (2)$$

Here, the SGS stress tensor τ^r_{ij} is modeled by a scale-dependent dynamic Smagorinsky model (Porté-Agel et al, 2000) and the flow is driven by a streamwise pressure gradient Π. For a statistically steady and

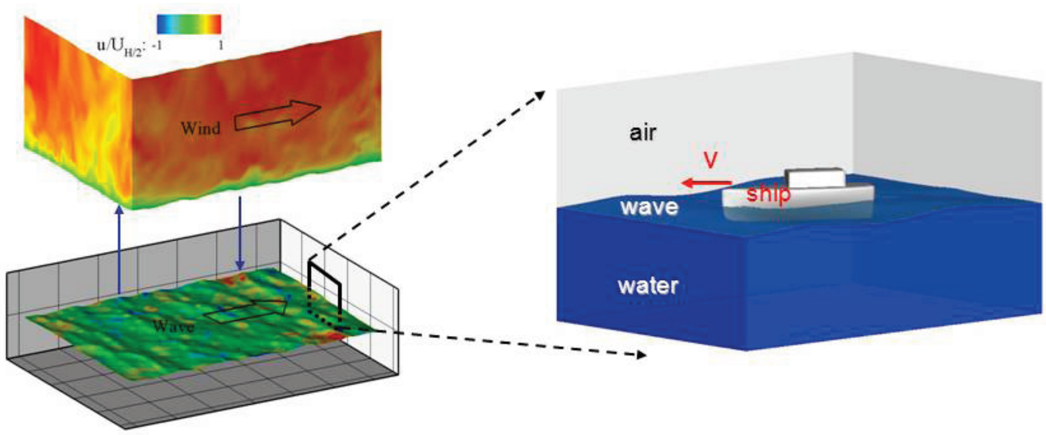

Figure 1: Sketch of the multiscale modeling strategy. On the left, the far-field simulation of wind and wave motions interacting with each other is shown. In the figure, the wind field is lifted up for better visualization. On the right, interactions of air and water motions with surface-piercing object such as a surface ship are simulated at local scales. The far-field simulation provides the inflow conditions of wind and waves to the near-field simulation.

fully developed flow,

$$\Pi = -\frac{\rho_a u_*^2}{\overline{H}} , \tag{3}$$

where $\overline{H}$ is the mean height of the computational domain, and u_* is the friction velocity of the turbulent wind near the wave surface. For the problem considered in this study, the Reynolds number is sufficiently high so that the molecular viscous term is neglected.

The lateral boundaries are treated as periodic. The top boundary of the simulation domain is rigid and free slip. The bottom of the domain is bounded by the water waves. A boundary-fitted grid system is used above the wave surface. The following algebraic mapping,

$$\tau = t \ , \ \xi = x \ , \ \psi = y \ , \ \zeta = \frac{z - \widetilde{\eta}(x,y,t)}{\overline{H} - \widetilde{\eta}(x,y,t)} \ , \tag{4}$$

is used to transfer the irregular wave surface-bounded domain in the physical space (x, y, z, t) to a right rectangular prism in the computational space (ξ, ψ, ζ, τ). Here, the height of the physical domain, $\widetilde{H}(x, y, t)$, is decomposed into the average height $\overline{H}$ and a wave induced variation $-\widetilde{\eta}(x, y, t)$.

The wind field is discretized by a pseudo-spectral method on a collocated grid in the horizontal direction, and a second-order central finite difference scheme on a staggered grid in the vertical direction. A standard logarithmic law-of-the-wall is used to imposed the proper sea-surface stress to the LES (Bou-Zeid et al, 2005). The flow field is advanced in time by a fractional step method.

The motion of the sea surface waves is simulated by a high-order spectral (HOS) method (Dommermuth and Yue, 1987). The HOS method simulates nonlinear waves using the Zakharov formulation (Zakharov, 1968), in which the wave motion is described by the surface elevation η and the surface potential Φ^s. Here, $\Phi^s = \Phi(x, y, z = \eta(x, y, t), t)$ with Φ being the velocity potential. The wave motion is governed by the kinematic and dynamic conditions at the sea-surface $z = \eta(x, y, t)$:

$$\frac{\partial \eta}{\partial t} + \nabla_h \eta \cdot \nabla_h \Phi^s - (1 + |\nabla_h \eta|^2) \frac{\partial \Phi}{\partial z} = 0 \ , \tag{5}$$

$$\frac{\partial \Phi^s}{\partial t} + g\eta + \frac{|\nabla_h \Phi^s|^2}{2} - \frac{1 + |\nabla_h \eta|^2}{2} \left(\frac{\partial \Phi}{\partial z} \right)^2 = 0 \ . \tag{6}$$

Here, $\nabla_h = (\partial/\partial x, \partial/\partial y)$ is the horizontal gradient; g is the gravitational acceleration.

In the simulation, Equations 5 and 6 are decomposed into individual wave modes and expanded to the nonlinear wave surface using a triple perturbation approach. A pseudo-spectral method is employed for the calculation of spatial derivatives and vector dot product. The wave field is advanced in time by a standard four-step fourth-order Runge–Kutta scheme. A complete review of the methodology, validation, and application of the HOS method is provided in Chapter 15 of Mei et al (2005).

The LES and HOS simulation are coupled through a fractional step method with two-way feedback (Yang and Shen, 2011b). In the simulation, the wind and wave fields have the same horizontal dimension.

At each time step, the HOS simulation provides the sea surface geometry and velocity to the wind LES, and the wind simulation advances in time and obtains air pressure distribution on the wave surface. The HOS simulation then uses the air pressure as the wind forcing in the dynamic free-surface boundary condition to advance the waves in time.

An important issue in LES of boundary layer flows over roughness surfaces such as the sea surface considered in the present problem is the modeling of SGS surface roughness. In LES of turbulent flows in marine atmospheric boundary layer and upper oceans, the waves falling below the grid resolution are treated as SGS surface roughness, which must be quantified accurately for the success of the simulations. The modeling of sea-surface roughness has been a long-standing problem in physical oceanography. In the literature, the roughness length scale is often parameterized by the Charnock relation or with sea-state scaling or wave-age scaling. However, previous studies have shown that these parameterizations may work for some sea conditions, but not in others. No universally consistent parameterization has been found yet. To resolve this issue, we have developed a novel dynamic sea-surface roughness model (Yang et al., 2013a, b). In the model, the roughness corresponding to the subgrid waves is expressed as a dimensionless model coefficient multiplied by the effective amplitude of the subgrid waves, which is modeled as a weighted integral of the subgrid wave spectrum. The model coefficient is determined dynamically based on the first-principles constraint that the total surface drag force or average surface stress must be independent of the LES filter scale. As a result, the variation of sea-surface roughness with wind and wave conditions can be captured faithfully in our simulations.

At each time step of the wind and wave simulation described above, the velocities of wind and waves are exported as inflow conditions to the local-scale simulation (see Figure 1) which is introduced in the next subsection.

2.2 Simulation of air and water ows around structure at local scales

In the near field surrounding the surface-piercing object, the air and water motions are described by the following filtered Navier–Stokes equations of incompressible multi-phase flows,

$$\begin{aligned}\frac{\partial \widetilde{u}_i}{\partial t} &= -\widetilde{u}_j\frac{\partial \widetilde{u}_i}{\partial x_j} - \frac{1}{\rho}\frac{\partial \widetilde{p}}{\partial x_i} + \frac{1}{\rho}\frac{\partial}{\partial x_j}(2\mu \widetilde{S}_{ij}) - \frac{1}{\rho}\frac{\partial \tau^r_{ij}}{\partial x_j} \\ &\quad + \frac{1}{\rho}\sigma\kappa\delta(d)n_i + G_i + \widetilde{f}_i \end{aligned} \tag{7}$$

and

$$\frac{\partial \widetilde{u}_i}{\partial x_i} = 0, \tag{8}$$

where $i = 1, 2, 3$, and $\widetilde{(\cdot)}$ denotes the filtered variables. Here $\widetilde{u}_i$ is the filtered fluid velocity; ρ and μ are respectively the density and dynamic viscosity of different fluids; $\widetilde{S}_{ij}$ is the filtered rate-of-strain tensor; τ^r is the trace-free part of the SGS stress tensor; $\widetilde{p}$ is the modified dynamic pressure including the trace of the SGS stress tensor; σ is the surface tension; κ is the curvature of interface; n_i is the unit outward normal vector at the wave surface; δ is the Dirac delta function; d is the normal distance to the surface; $G_i = (0, 0, g)$ is the gravity force, and $\widetilde{f}_i$ is a body force for the object using the immersed boundary method.

Finite difference schemes are used to discretize Equations 7 and 8 on a staggered Cartesian grid. The advective term $A = \widetilde{u}_j\partial\widetilde{u}_i\backslash\partial x_j$ at time step n is calculated by a linear combination of a 4th-order WENO scheme (Liu et al. 1994) and a standard 4th-order central scheme, i.e.

$$A^n = \alpha(A^n)_{\text{central}} + (1-\alpha)(A^n)_{\text{WENO}} \tag{9}$$

where α is a weighting coefficient set to be 0.8 in this study. We use this hybrid scheme to take advantage of the suppressing of non-physical oscillations by the WENO scheme and at the same time to reduce its numerical dissipation. If the central scheme is used alone, numerical oscillations occur where velocity gradients are large.

The SGS stress term τ^r_{ij} is modeled by a renormalization group (RNG) method (Yakhot and Orszag, 1986; Yakhot et al, 1989) as

$$\tau^r_{ij} = -2\frac{\mu^{SGS}}{\rho}\widetilde{S}_{ij}. \tag{10}$$

Here,

$$\begin{aligned}\mu^{SGS} + \mu = \mu\Bigg[1 + \left(\frac{\mu_s^2(\mu^{SGS}+\mu)}{\mu^3} - C\right) \\ \times H\left(\frac{\mu_s^2(\mu^{SGS}+\mu)}{\mu^3} - C\right)\Bigg]^{1/3}, \end{aligned} \tag{11}$$

where $H(x)$ is the Heaviside step function, defined as $H(x) = 1$ if $x > 0$ and $H(x) = 0$ otherwise; $\mu_s = \rho C_{RNG} \triangle^2 \sqrt{2\widetilde{S}_{ij}\widetilde{S}_{ij}}$, in which the Smagorinksy constant $C_{RNG} = 0.0062$ and the filter width $\triangle = (\triangle_x \triangle_y \triangle_z)^{1/3}$ with $\triangle_x$, $\triangle_y$, and $\triangle_z$ being the local grid sizes in x-, y-, and z-directions, respectively; and C is a constant set to be 75 (Yakhot and Orszag, 1986).

Equations 7 and 8 are advanced in time by a fractional-step method (Kim and Moin, 1985): first, the momentum equation without the pressure term is integrated in time explicitly; then a pressure Poisson equation is solved by a bi-conjugate gradient stabilized (Bi-CGSTAB) method (van der Vorst, 1992; Xiao, 2001) to obtain pressure update satisfying mass conservation. At each time step, a second-order Runge-Kutta method is used.

The multi-phase flows of air and water are distinguished in a fixed Cartesian grid by a level-set method (Sussman et al, 1994; Osher and Fedkiw, 2001). The two fluids and their interface are identified by a signed distance function ϕ as

$$\phi(\mathbf{x}) = \begin{cases} d & \text{water} \\ 0 & \text{interface} \\ -d & \text{air} \end{cases} . \tag{12}$$

It is clear that the air–water interface is represented by the zero level of ϕ. Consequently, the density ρ and viscosity μ in Equation 7 are written in the form of

$$\rho(\phi) = \rho_a(1 - H(\phi)) + \rho_w H(\phi), \tag{13}$$

$$\mu(\phi) = \mu_a(1 - H(\phi) + \mu_w H(\phi)). \tag{14}$$

Here, ρ_a and μ_a are respectively the density and viscosity of air, ρ_w and μ_w are density and viscosity of water, and $H(\phi)$ is the Heaviside step function.

The evolution of the distance function ϕ are obtained by solving an advection equation (Sussman et al, 1994)

$$\frac{\partial \phi}{\partial t} + \mathbf{u} \cdot \nabla \phi = 0, \tag{15}$$

where $\mathbf{u}$ is the velocity vector of the fluid. Since the signed distance property may not be satisfied in time, i.e. $\nabla \phi \neq 1$, a reinitialization procedure as following is used (Sussman et al, 1998) as a correction without changing the position of its zero level

$$\frac{\partial \phi_c}{\partial \tau} + sign(\phi)(|\nabla \phi| - 1) = 0. \tag{16}$$

Here, ϕ_c is the corrected function of ϕ and τ is the artificial time. The steady solutions of Equation 16 are the desired distance functions.

By using the level-set method, the multi-phase flows with high density and viscosity ratios can be treated in a fully coupled way and the air–water interface is traced implicitly and dynamically. Moreover, another advantage of the level-set method is that the unit outward normal $\mathbf{n}$ and the curvature κ of the interface can be easily obtained by

$$\mathbf{n} = \frac{\nabla \phi}{|\nabla \phi|} \tag{17}$$

and

$$\kappa = \nabla \cdot \mathbf{n} = \nabla \cdot \frac{\nabla \phi}{|\nabla \phi|}, \tag{18}$$

where ∇ denotes the spacial gradient of a scalar, and "$\cdot$" is the dot product of two vectors.

To model the effect of the presence of the object on the surrounding fluid motions, we employ an immersed boundary method (Peskin, 2002; Mittal and Iaccarino, 2005). In this method, boundary conditions are not explicitly prescribed at the solid boundaries, but realized by body forces distributed in the fluid domain that serve as source terms $\widetilde{f}_i$ in the momentum equation 7. Therefore, the solid boundaries are "immersed" in the flow field and the boundary conditions are satisfied. The immersed boundary method can be categorized into two groups by the ways of calculation and distribution of the body forces: i) continuous forcing approach, which take the forcing terms into the continuous governing equations before discretization, and ii) discrete forcing approach, which discretizes and solves the momentum equations without consideration of the forcing terms first, and then uses the forcing terms to correct the boundary conditions. In this study, the latter is used because it allows direct control of numerical accuracy and thus a sharp interface can be captured (Mittal and Iaccarino, 2005). The IB method does not require a body-fitted mesh. As a result, they have the advantage in simulations involving complex structures by using a simple Cartesian grid.

Referring to Figure 2, the calculation and distribution of $\widetilde{f}_i$ are briefly described below. First, fluid grid points immediately outside the object are tagged and denoted as the forcing points $\mathbf{x}_f$. The points inside the object are denote as inner points. Second, the desired velocities $\widetilde{u}_i^d$ at the forcing points and inner points are calculated. For high Reynolds number flows, the standard interpolation is not applicable at the forcing points, since the forcing points are located outside of the the viscous sub-layer, i.e. $y^+ >> 5$. Therefore, a wall-layer modeling treatment is required to impose the velocity boundary conditions properly. As shown in Figure 2 (b), for a forcing point $\mathbf{x}_f$, its normal projection point $\mathbf{x}_s$ on the surface Γ_b is found as well as a probe point $\mathbf{x}_p$ along the outward normal direction with the same distance. The velocity $\widetilde{u}_i^p$ at $\mathbf{x}_p$ is interpolated from its surrounding grid points since they are less affected by the surface. Then $\widetilde{\mathbf{u}}_p$ is decomposed into a normal component $\widetilde{\mathbf{u}}_n$ and a tangential component $\widetilde{\mathbf{u}}_t$. Next, the wall shear stress τ_w based on $\widetilde{\mathbf{u}}_t$ is estimated by the Werner–Wengle model (Werner and Wengle, 1991; Hassan and Barsamian, 2001; Grigoriadis et al, 2003, 2004) as

$$|\tau_w| = \frac{2\mu|\widetilde{\mathbf{u}}_t|}{\Delta y} \quad \text{for} \quad |\widetilde{\mathbf{u}}_t| \le \frac{\mu}{2\rho\Delta y} A^{\frac{2}{1-B}}, \tag{19}$$

$$|\tau_w| = \rho[\frac{1-B}{2} A^{[(1+B)/(1-B)]}(\frac{\mu}{\rho\Delta y})^{1+B} + \frac{1+B}{A} \times(\frac{\mu}{\rho\Delta y})^B|\widetilde{\mathbf{u}}_t|]^{2/(1+B)} \quad \text{for} \quad |\widetilde{\mathbf{u}}_t| > \frac{\mu}{2\rho\Delta y} A^{\frac{2}{1-B}}, \tag{20}$$

where $A = 8.3$, $B = 1/7$, and Δy is the distance from the surface to $\mathbf{x}_p$. This model yields to the linear law-of-the-wall for the points inside the viscous sublayer and the power law $u^+ = A(y^+)^B$ for the points outside. Once τ_w is obtained, the tangential velocity component at the forcing point $\mathbf{x}_f$ is calculated from the inverse expressions of (19) and (20) using the distance $\Delta y = d$. The normal velocity component at $\mathbf{x}_f$ is calculated by linear interpolation. The desired velocities at the inner points are all set to zero. Lastly, the forcing terms $\widetilde{f}_i$ at time step n is calculated at the forcing points and inner points by

$$\widetilde{f}_i^n = \frac{\widetilde{u}_i^d - \widetilde{u}_i^n}{\triangle t} - [RHS_i^n], \tag{21}$$

where $[RHS_i^n]$ is the discretized form of the right hand side of Equation (7) without the forcing terms.

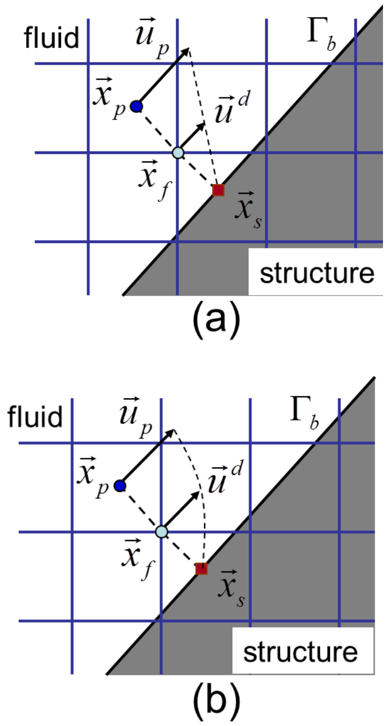

Figure 2: Sketch of the immersed boundary method (a) without wall-layer modeling, (b) with wall-layer modeling. The blue filled circle denotes the probe point, the blue hollow circle denotes the forcing point, and the red square is the projection point on the surface. The grey shadow zone represents the inner regime of the object, and Γ_b is the surface of the object.

3 RESULTS

In this section, two test cases are first presented as validations of the numerical method. Next, the canonical problem of wind blowing over a surface-piercing rectangular prism in a wave field is discussed. Finally, preliminary result of wind and waves past a Wigley ship model is shown.

As shown in the sketch in Figure 3, we consider a turbulent boundary layer flow past a surface-mounted cube to test the LES and the immersed boundary method. The Reynolds number is 10^5 based on the height of the structure h and the mean upstream velocity at that height U (Castro and Robins, 1977;

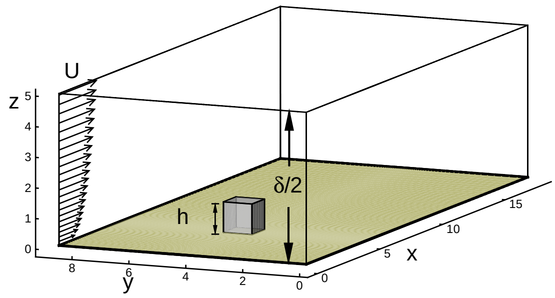

Figure 3: Sketch of the simulation of boundary layer flow around a cube mounted on a flat plate.

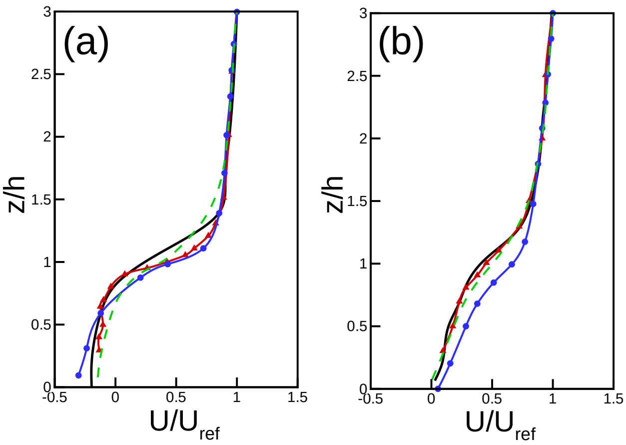

Figure 4: Comparisons of vertical profiles of mean streamwise velocity on the vertical central plane at (a) $(x-x_0)/h = 1.0$, and (b) $(x-x_0)/h = 2.0$. Here, x_0 is the streamwise coordinate of the center of the cube, U_{ref} is the mean velocity at the height of $z/h = 3$. The black solid line is the current result, the red symbol denotes data from Castro & Robins (1977), the blue symbol is data from Vasilic-Melling (1976), and the green dash line is data from from Paterson and Apelt (1990).

Murakami et al, 1987). The inflow is imported from a simulated fully-developed turbulent boundary layer without the presence of the cube, and radiation condition is applied on the outflow boundary. A periodic condition is used on the spanwise boundaries. Non-slip and free-slip boundaries are assumed for the ground and top boundaries, respectively.

Figure 4 compares the mean streamwise velocity profiles at two locations behind the cube on the vertical central plane between our simulation result and previous measurement and simulation data from literature. The present result agrees well with those from literature. The free shear layer separates from the rear of the cube and leads to a reversed flow as seen in all the data at the location $(x-x_0)/h = 1.0$ in Figure 4(a). The deviation increases in the region $0.8 < z/h < 1.3$ due to the relatively coarse grid used at the shear layer. At the location $(x-x_0)/h = 2.0$ in Figure 4(b), the reversed streamwise velocity disappears, indicating that the flow reattaches to the ground.

Figure 5 compares the pressure coefficient distributions along the vertical and horizontal central lines of the cube between our simulation results and data reported in literature. The pressure coefficient is defined as

$$Cp = \frac{p - p_r}{\frac{1}{2}\rho_a U_h^2}. \tag{22}$$

Here, p is the pressure, p_r is the pressure at a reference point, ρ_a is the density of air, and U_h is the mean streamwise velocity averaged over the horizontal plane at the height h. In all the cases, the highest pressure occurs at the stagnation point on the frontal face, and the lowest pressure is located where flow separates at the leading edges of the roof and side walls. The present simulation shows good agreement with previous experimental and numerical data especially on the frontal face, but the deviation between different sets of data increases on the faces where flow separates. While the pressure distribution is sensitive to the turbulence intensity and surface roughness effects (Richards et al, 2001), the figure shows that the present result agrees reasonably well with the data from literature.

Next, we examine the accuracy of wind-and-wave simulation in far field. As pointed out above, the simulation of wind and waves in far field is crucial to provide physical inflow conditions for local-scale simulation of air and water motions surrounding the object. Here, a turbulent wind field is simulated over a wave field that has the JONSWAP (Joint North Sea Wave Project) spectrum as

$$S(\omega) = \frac{\alpha g^2}{\omega} \exp[-\frac{4}{5}(\frac{\omega_p}{\omega})^4]\gamma^r, \tag{23}$$

with

$$r = \exp[-\frac{(\omega-\omega_p)^2}{2\sigma^2\omega_p^2}]. \tag{24}$$

Here,

$$\alpha = 0.076(\frac{U_{10}^2}{Fg})^{0.22}, \quad \omega_p = 22(\frac{g^2}{U_{10}F}),$$
$$\gamma = 3.3, \quad \sigma = \begin{cases} 0.07 & \omega \le \omega_\mathrm{p} \\ 0.09 & \omega > \omega_\mathrm{p} \end{cases}, \tag{25}$$

where ω and ω_p are respectively the angular frequency and angular frequency at the spectrum peak, U_{10} is the mean wind speed at the height of 10m above the sea surface, and F is the fetch (Hasselmann et al, 1973). It is clear that the spectrum varies with wind velocity and fetch. In the simulation case shown, the parameters are chosen as: $U_{10} = 9.5$m/s, $F = 112$km, and the friction velocity $u_* = \sqrt{\tau_w/\rho_a}$ is about 0.36m/s, where τ_w is the mean shear stress at the water surface. Under this wind condition, the wavelength at the spectrum peak is $\lambda_p \approx 63.3$m, and the significant wave

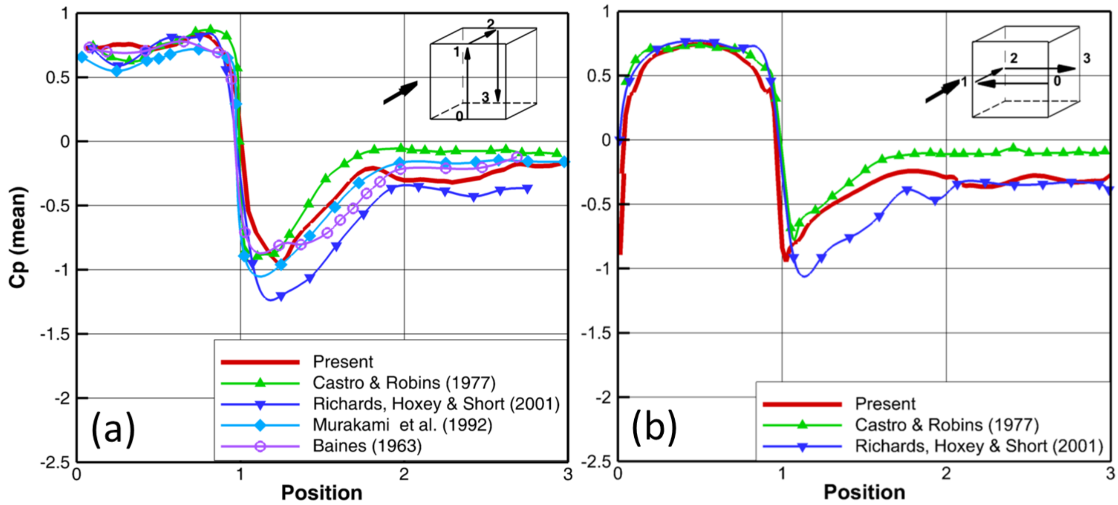

Figure 5: Comparisons of distribution of pressure coefficient (a) along the vertical central line of the cube, and (b) along the horizontal central line of the cube.

height is $H_s \approx 2.18$m. The simulation is performed in a domain of 1000m × 500m × 500m in streamwise (x), vertical (z), and spanwise (y) directions, respectively. A uniform grid is used with the resolution of $192 \times 128 \times 128$. The wave field has the same horizontal size and resolution. Note that the HOS method does not require a vertical grid.

Figure 6 shows an instantaneous wind-and-wave field from the simulation. The complex structure of turbulence is seen in the wind field above the waves, which are irregular and have broadband spectrum. A common way to check the performance of wind–wave simulations is to quantify the sea-surface drag on wind and the momentum transfer between wind and waves. To do this, we transform the surface elevation and the pressure obtained from the LES and HOS simulation to wavenumber space. The air pressure acting on the sea surface is thus decomposed into different wave modes, corresponding to different wavenumber k.

The temporal rate of energy transfer from the wind to the wave at wavenumber k is quantified as (Donelan et al, 2006)

$$\gamma(k) = \frac{\rho_w}{\rho_a} \frac{1}{\omega e} \frac{\mathrm{d}e}{\mathrm{d}t} = \left(\frac{u_*}{c}\right)^2 \beta \, . \tag{26}$$

Here, for the k-th mode, $e = \rho_w g [a(k)]^2/2$ is the wave energy density, with $a(k)$ being the corresponding wave amplitude; $\omega = \sqrt{gk}$ is the corresponding angular frequency under deep water condition; β is the wave growth rate parameter (Miles, 1957, 1993); and ρ_a and ρ_w are the densities of air and water, respectively. The growth rate parameter β is related to the wind pressure through (see e.g. Donelan et al, 2006)

$$\beta(k) = \frac{2}{[a(k)k]^2} \frac{1}{A} \iint_A \frac{p_k}{\rho_a u_*^2} \frac{\partial \eta_k}{\partial x} \, \mathrm{d}x\mathrm{d}y \, . \tag{27}$$

Here, p_k and η_k are the air pressure at the wave surface and surface displacement for the k-th wave mode, respectively. Figure 7 shows the dependence of the dimensionless temporal growth rate γ/ω on the wind–wave velocity ratio u_*/c. Comparison between our simulation results and data from the literature shows good agreement.

The two simulation cases above examine different aspects of the simulation method. Next, we apply this numerical tool to investigate the canonical problem of wind and waves passing a surface-piercing object of rectangular prism. Referring to Figure 1 with the ship replaced by a rectangular prism, the computational domain for the near-field simulation has the size of 600m in the streamwise direction and 300m in both the vertical and spanwise directions. The object with the height of $2h = 100$m has an aspect ratio of length:height:width=1:2:1, where h is the height of the object above the mean water level. A Cartesian grid with the resolution of $192 \times 128 \times 128$ in streamwise, vertical and spanwise directions is used. The grid is clustered near the object and the wave surface. The center of the object is located at $(x_0, y_0, z_0) = (3h, 3h, 3h)$ in the computational domain. Periodic boundary condition is used

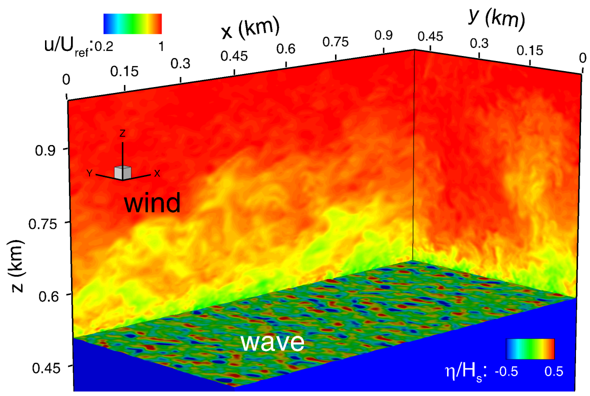

Figure 6: An instantaneous turbulent wind field above a JONSWAP wave field. The contours of water surface elevations η normalized by the significant wave height H_s are plotted on the wave surface, and the contours of streamwise velocity of wind u normalized by the mean velocity at the top of the domain U_{ref} are shown on the spanwise and outflow boundaries.

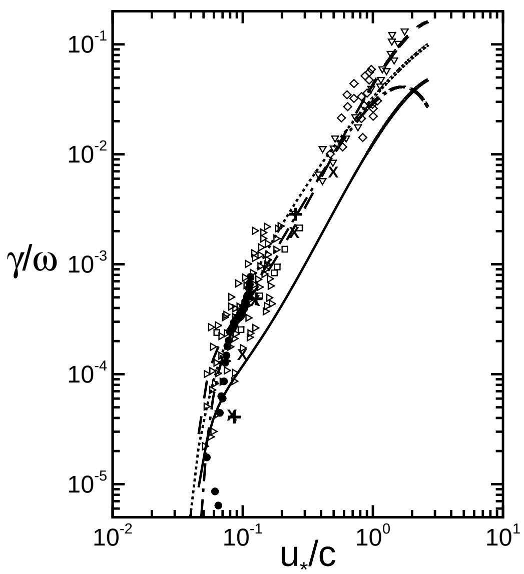

Figure 7: Dependence of the wave growth rate γ (normalized by angular frequency ω) on the wind–wave velocity ratio u_*/c and comparison of the current LES with previous experiments and simulations. Experimental data compiled by Plant (1982) are indicated by open symbols. Values predicted by various wind-wave theories are indicated by lines: ——, Miles (1957); – –, Janssen (1991); and – · –, Miles (1993). Values given by the parameterization of Donelan et al (2006) are indicated by ···. DNS results from Sullivan et al (2000) are marked by +. DNS results from Kihara et al (2007) are marked by ×. The current result is indicated by •.

on the side boundaries. Both the bottom and top boundaries are treated as slip-free. The inflow is obtained from a far-field wind–and–wave coupled simulation using the method discussed in Section 2.1, and a radiation boundary condition is used at the outflow boundary to suppress numerical reflection.

Three wind-wave conditions are considered. Case 1 has the JONSWAP wind-waves described earlier. Cases 2 and 3 have a swell of wavelength 200m superimposed to the JONSWAP waves, with the swell steepness being $ak = 0.1$ and $ak = 0.15$ in cases 2 and 3, respectively. The swells and the dominant JONSWAP waves propagate in the same direction normal to the object. For wind–wave interactions, an important parameter to quantify the relative motion of waves with respect to wind is called the wave age, defined as the ratio of the wave celerity to the characteristic wind velocity. For the JONSWAP waves and the swells used in this paper, the wave ages are

$$\frac{C_{peak}}{U_{10}} = 1.05, \quad \frac{C_{swell}}{U_{10}} = 1.86. \tag{28}$$

Here, C_{peak} is the wave celerity at the peak of the local wind-waves, C_{swell} is the celerity of the swell, and U_{10} is the mean velocity of wind at the height of 10m above the mean sea level.

The wind drag D_{wind} acting on the object is calculated by the area integration of the air pressure on the frontal and rear faces of the prism. Viscous force is neglected because it is much smaller. The wind drag coefficient is defined as

$$Cd_{wind} = \frac{D_{wind}}{\frac{1}{2}\rho_a U_h^2}, \tag{29}$$

where U_h is the mean streamwise velocity averaged over the plane at the height of the object roof. Temporal variations of Cd_{wind} and the mean incident wave surface elevation η_{mean} for the three cases are shown in Figure 8. Here, η_{mean} is defined as the averaged surface elevation of the wave arriving at the frontal face of the object. For Case 1, the significant wave height is used for the normalization of η_{mean}, while for Cases 2 and 3 the corresponding swell height is used. Figure 8 shows that the wind drag coefficient oscillates in time for all the three cases, and the oscillation is strongly correlated with the swell phase as shown in Figures 8(b) and (c). For Case 1 shown in Figure 8(a), the dependence of the wind drag coefficient on the wave phase is less obvious because of the lack of dominant wave component.

We further perform phase averaging for the temporal data of Cd_{wind} and η_{mean} of Case 2 and 3, and

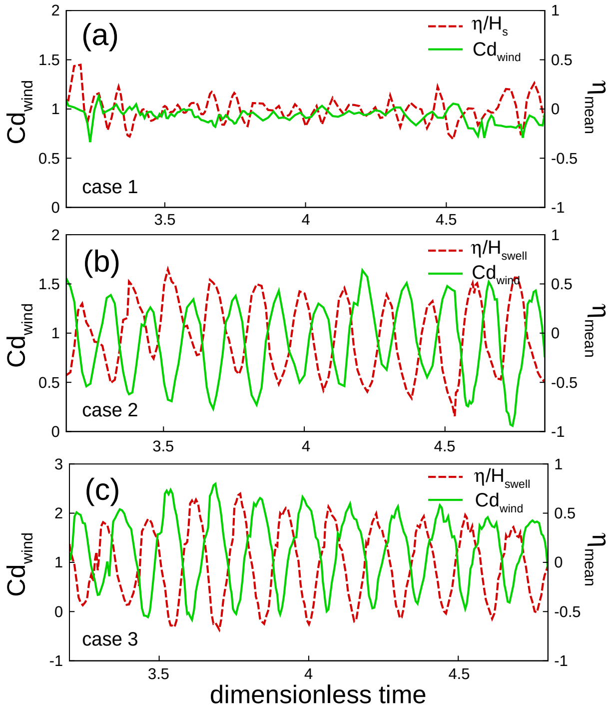

Figure 8: Time variations of wind drag coefficient and mean incident wave surface elevation in front of the object of (a) Case 1, (b) Case 2, and (c) Case 3.

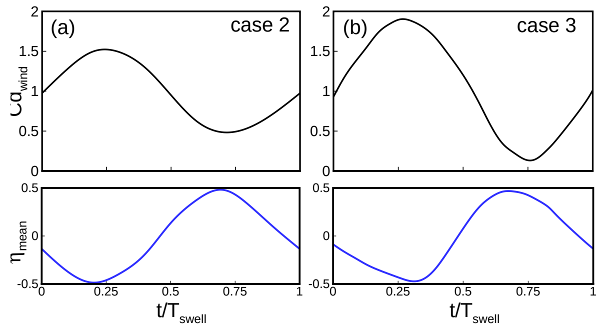

Figure 9: Phase-averaged wind drag coefficient and mean incident wave surface elevation in front of the object of (a) Case 2 and (b) Case 3. T_{swell} is the wave period of the swell.

plot the result in Figure 9. The correlation coefficient between Cd_{wind} and η_{mean} is about -0.96 for Case 2 and -0.94 for Case 3. Figure 9 also shows that the variation of the phase-averaged Cd_{wind} of Case 3 is approximately 48% larger than that of Case 2, because the swell magnitude is larger in Case 3, although their mean values are almost the same.

As discussed earlier, the correlation between Cd_{wind} and η_{mean} is relatively weak for Case 1 compared with Cases 2 and 3 where swell is present. Nevertheless, the instantaneous flow fields plotted in Figure 10 still indicate strong variation of Cd_{wind} with incident waves. The figure shows that the wave motion causes appreciable variation of the pressure distribution on the frontal face, and the pressure variation is more significant near the wave surface. As shown by Sullivan et al (2000) and Yang and Shen (2010), the effect of a wave on the air can reach to a height approximately one wavelength above the water surface. Considering that the wavelength at the JONSWAP spectrum peak is 63.3m, which is comparable to the height of the object above the water (50m), it is not surprising that the wind pressure on the entire frontal face is influenced by the wave. Also as expected, this effect deceases quickly from the lower part of the object to the upper part. The reason that the statistical result in Figure 8(a) does not show much coherence between Cd_{wind} and η_{mean} is because there are many wave components of comparable magnitude influencing the air motion simultaneously. From Figure 10, we can see that instantaneously the energy-containing wave components still cause large variations in the air pressure distribution on the object surface.

On the other hand, as shown in Figures 8(b) and (c), the correlation between Cd_{wind} and η_{mean} is significant when a swell is present. Since the swell considered in this study has a wavelength of 200m, much larger than the object height, the object is located in the region where the air is strongly influenced by the swell. The swell behaves like a large monochromatic wave while the local JONSWAP waves are much smaller in size. Therefore, the correlation is strong and clear.

Finally, we present example results of our recent preliminary simulations of wind and waves past a Wigley ship hull with simplified superstructure, to illustrate the capability and potential application of the simulation tool developed in this study. Figure 11 uses streamlines to illustrate the air flows around a ship in a head wind. Figure 12 shows an example of the wind velocity and pressure coefficient in the air at different heights relative to the ship hull and superstructure. From such data, detailed flow field and spatial variations of air pressure acting on the ship surface can be obtained. For instance, in Figure 12, the left panel shows a maximum pressure coefficient value of 0.38 at the stagnation point on the ship hull, while the right panel shows a maximum value of 0.57 on the superstructure because the

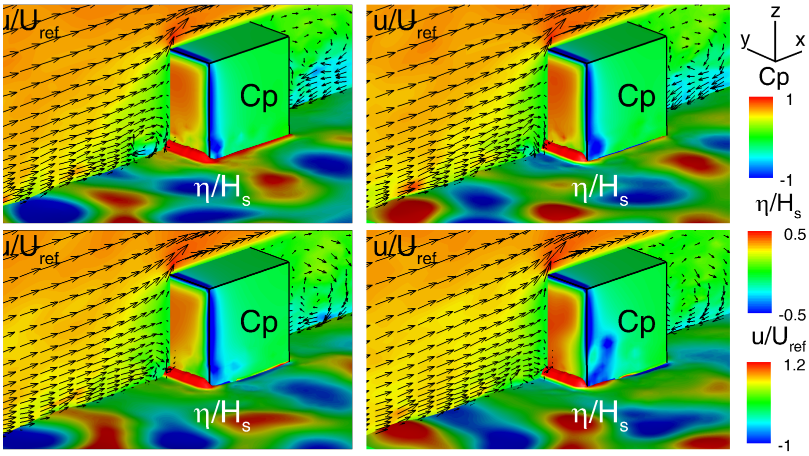

Figure 10: Four instantaneous flow fields around the object for Case 1. The contours are: pressure coefficient Cp on the surface of the object, water surface elevations η normalized by the significant wave height H_s on the wave surface, and the streamwise velocity of wind u (plotted on the central vertical plane) normalized by the mean streamwise velocity U_{ref} at the top the domain.

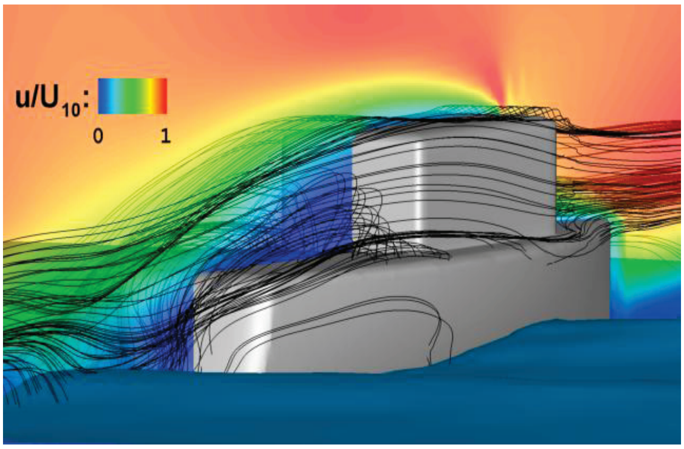

Figure 11: 3D view of instantaneous air flow field around a ship hull in head wind condition.

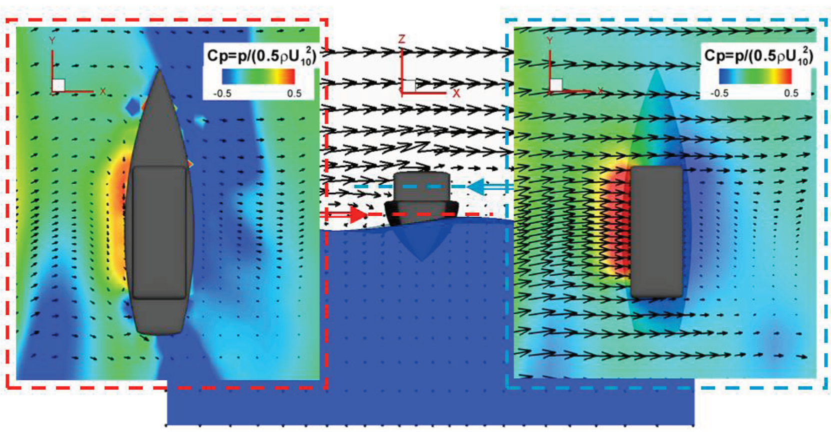

Figure 12: Top and rear views of instantaneous air flow field around a ship hull in beam wind condition.

wind is stronger at higher altitude. The wind profile variation is a complex problem in marine atmosphere boundary layer study by itself. To obtain accurate result of wind loads for ship hydrodynamics applications, it is essential to capture the wind profile in wave environment. Another interesting result is that it is found from our simulation that the wind loads varies significantly in time. At different phases of a swell arriving at the ship, up to 35% variation in the wind loads have been observed in our simulation data. Such large oscillation in wind loads is expected to play an important role in ship motion and should be taken into account in study of ship operation and control.

4 CONCLUSIONS

Wind loads are important in many naval applications. The wind field at sea is a complex system dynamically coupled with the wave field including windseas and swells. To obtain an improved modeling capability for and a deeper understanding of wind loads on surface ships, there is a critical need for the development of advanced numerical tool for the simulation of coupled wind and wave motions and their loads on the ships. In this study, we have developed a multiscale modeling approach for the interactions among wind, waves, and surface-piercing structure. Because the evolution of a realistic ocean wave field, which contains a large number of wave modes interacting with each other through nonlinear processes, is a process occurring over a relatively long distance, we simulate the dynamic interaction between wind and waves in the far field. The solution obtained faithfully captures the physics of realistic wind and wave interaction, and is then fed to near-field simulation of air, water, and structure interactions. The simulation results indicate that the waves have an appreciable effect on the wind loads on surface-piercing structures. Therefore, for accurate quantification of wind loads in realistic marine atmosphere and wave environment for naval applications, it is essential for future simulation studies to have the capability of dynamically modeling the coupling among wind, wave, and ship motions, for which the numerical method developed in this study can serve as useful simulation tool in the future.

References

[1] Aage, C., "Wind coefficients for nine ship models," Report No. A-3, 1971, Hydro and Aerodynamic Laboratory, Lyngby, Denmark.

[2] Aage, C., Hvid, S.L., Hughes, P.H., and Leer-Andersen, M., "Wind loads on ships and offshore structures estimated by CFD," *Proceedings of the 8th International Conference on Behaviour of Offshore Structures (BOSS'97)*, Delft, Netherlands, 1997, pp. 237-251.

[3] Baines, W.D., "Effects of velocity distribution on wind loads and flow patterns on buildings," *Proceedings of the Symposium on Wind Effects on Buildings and Structures*, Vol. 16, Teddington, UK, 1963.

[4] Belcher, S.E. and Hunt, J.C.R., "Turbulent flow over hills and waves," *Annual Review of Fluid Mechanics*, Vol. 30, 1998, pp. 507-538.

[5] Blendermann, W., "Ship shape and wind loads - Correlation and regression analysis of wind tunnel tests on ship models (Schiffsform und Windlast - Korrelations- und Regressionsanalyse von Windkanalmessungen am Modell)," Report No. 533, 1993, Institut für Schiflbau der Universität Hamburg.

[6] Blendermann, W., "Parameter identification of wind loads on ships," *Journal of Wind Engineering and Industrial Aerodynamics*, Vol. 51, 1994, pp. 339-351.

[7] Blendermann, W., "Estimation of wind loads on ships in wind with a strong gradient," *Proceedings of the 14th International Conference on Offshore Mechanics and Arctic Engineering (OMAE)*, New York: ASME, Vol. 1, 1995, pp. 271-277.

[8] Blendermann, W., "Ships may encounter high wind loads-a statistical assessment," *Proceedings of Institution of Mechanical Engineers, Part M: Journal of Engineering for the Maritime Environment*, Vol. 218, 2004, pp. 1-10.

[9] Bou-Zeid, E., Meneveau, C., and Parlange, M., "A scale-dependent lagrangian dynamic model for large eddy simulation of complex turbulent flows," *Physics of Fluids*, Vol. 17, 2005, 025105.

[10] Brizzolara, S. and Rizzuto, E., "Wind heeling moments on very large ships. Some insights through CFD results," *Proceedings of the 9th International Conference on the Stability of Ships*

and Ocean Vehicles, Rio de Janeiro, Brazil, Vol. 2, 2006, pp. 781-793.

[11] Castro, I.P. and Robins, A.G., "The flow around a surface-mounted cube in uniform and turbulent streams," *Journal of Fluid Mechanics*, Vol. 79, Part 2, 1977, pp. 307-335.

[12] Dommermuth, D.G. and Yue, D.K.P., "A high-order spectral method for the study of nonlinear gravity waves," *Journal of Fluid Mechanics*, Vol. 184, 1987, pp. 267-288.

[13] Donelan, M.A., Babanin, A.V., Young, I.R., and Banner, M.L., "Wave-follower field measurements of the wind-input spectral function. Part II: Parameterization of the wind input," *Journal of Physical Oceanography*, Vol. 36, 2006, pp. 1672-1689.

[14] Fujiwara, T. and Nimura, T., "New estimation method of wind forces acting on ships on the basis of mathematical model," *Proceedings of the Fifteenth International Offshore and Polar Engineering Conference*, Seoul, Korea, 2005, pp. 82-89.

[15] Grigoriadis, D.G.E., Bartzis, J.G., and Goulas, A., "LES of the flow past a rectangular cylinder using the immersed boundary concept," *International Journal of Numerical Methods in Fluids*, Vol. 41, 2003, pp. 615-632.

[16] Grigoriadis, D.G.E., Bartzis, J.G., and Goulas, A., "Efficient treatment of complex geometries for large eddy simulations of turbulent flows," *Computers and Fluids*, Vol. 33, 2004, pp. 201-222.

[17] Haddara, M.R., Guedues Soares, C., "Wind loads on marine structures," *Marine Structures*, Vol. 12, 1999, pp. 199-209.

[18] Hassan, Y.A. and Barsamian, H.R., "New-wall modeling for complex flows using the large eddy simulation technique in curvilinear coordinates," *International Journal of Heat and Mass Transfer*, Vol. 44, 2001, pp. 4009-4026.

[19] Hasselmann K., Barnett, T.P., Bouws, E., Carlson, H., Cartwright, D.E., Enke, K., Ewing, J.A., Gienapp, H., Hasselmann, D.E., Kruseman, P., Meerburg, A., Mller, P., Olbers, D.J., Richter, K., Sell, W., and Walden, H., "Measurements of wind-wave growth and swell decay during the Joint North Sea Wave Project (jonswap)," *Deutsche Hydrographische Zeitschrift*, Vol. 8, No. 12, 1973.

[20] Isherwood, R.M., "Wind resistance of merchant ships," *Transactions of the Royal Institution of Naval Architects*, Vol. 114, 1972, pp. 327-338.

[21] Janssen, P.A.E.M., "Quasi-linear theory of wind-wave generation applied to wave forecasting," *Journal of Physical Oceanography*, Vol. 21, 1991, pp. 1631-1642.

[22] Kihara, N., Hanazaki, H., Mizuya, T., and Ueda, H., "Relationship between airflow at the critical height and momentum transfer to the traveling waves," *Physics of Fluids*, Vol. 19, 2007, 015102.

[23] Kim, J. and Moin, P., "Application of a fractional-step method to incompressible Navier-Stokes equations," *Journal of Computational Physics*, Vol. 59, 1985, pp. 308-323.

[24] Lee, T.S. and Low, H.T., "Wind effects on offshore platforms a wind tunnel model study," *Proceedings of the Third International Offshore and Polar Engineering Conference*, Singapore, 1993, pp. 446-470.

[25] Liu, X., Osher, S., and Chan, T., "Weighted essentially non-oscillatory schemes," *Journal of Computational Physics*, Vol. 115, 1994, pp. 200-212.

[26] Low, C.T., *Boat Docking (Close Quarters Maneuvering for Small Craft)*, Harvey Island Enterprises, Brockville, 1997.

[27] Matsumoto, K., Tanaka, Y., Hirota, K., Usami, S., and Takagishi, K., "Reduction of wind force acting on ships," *Journal of the Kansan Society of Naval Architects*, Vol. 240, 2003, pp. 115-121.

[28] Mei, C.C., Stiassnie, M., and Yue, D.K.P., *Theory and Applications of Ocean Surface Waves. Part 2: Nonlinear Aspects*, World Scientific, Singapore, 2005.

[29] Miles, J.W., "On the generation of surface waves by shear flows," *Journal of Fluid Mechanics*, Vol. 3, 1957, pp. 185-204.

[30] Miles, J.W., "Surface-wave generation revisited," *Journal of Fluid Mechanics*, Vol. 256, 1993, pp. 427-441.

[31] Mittal, R. and Iaccarino, G., "Immersed boundary methods," *Annual Review of Fluid Mechanics*, Vol. 37, 2005, pp. 239-261.

[32] Mousaviraad, S.M., "CFD prediction of ship response to extreme winds and/or waves," PhD thesis, Univeristy of Iowa, 2010.

[33] Murakami, S., Mochida, A., and Hibi, K., "Three-dimensional numerical simulation of air flow around a cubic model by means of large eddy simulation," *Journal of Wind Engineering and Industrial Aerodynamics*, Vol. 25, 1987, pp. 291-305.

[34] Murakami, S., Mochida, A., Hayashi, Y., and Sakamoto, S., "Numerical study on velocity-pressure filed and wind forces for bluff by k-e, ASM and LES," *Journal of Wind Engineering and Industrial Aerodynamics*, Vol. 41-44, 1992, pp. 2841-2852.

[35] Osher, S. and Fedkiw, R.P., "Level set methods: an overview and some recent results," *Journal of Computational Physics*, Vol. 169, 2001, pp. 463-502.

[36] Paterson, D.A. and Apelt, C.J., "Simulation of flow past a cube in turbulent boundary layer," *Journal of Wind Engineering and Industrial Aerodynamics*, Vol. 35, 1990, pp. 149-176.

[37] Peskin, C.S., "The immersed boundary method," *Acta Numerica*, Vol. 11, 2002, pp. 479-517.

[38] Plant, W.J., "A relationship between wind stress and wave slope," *Journal of Geophysical Research*, Vol. 87, 1982, pp. 1961-1967.

[39] Popinet, S., Smith, M., and Stevens, C., "Experimental and numerical study of the turbulence characteristics of air flow around a research vessel," *Journal of Atmospheric and Oceanic Technology*, Vol. 21, 2004, pp. 1575-1589.

[40] Porté-Agel, F., Meneveau, C., and Parlange, M.B., "A scale-dependent dynamic model for large-eddy simulation: application to a neutral atmospheric boundary layer," *Journal of Fluid Mechanics*, Vol. 415, 2000, pp. 261-284.

[41] Richards, P.J., Hoxey, R.P., and Short, L.J., "Wind pressure on a 6 m cube," *Journal of Wind Engineering and Industrial Aerodynamics*, Vol. 89, 2001, pp. 1553-156.

[42] Sethian, J.A. and Smereka, P., "Level set methods for fluid interfaces," *Annual Review of Fluid Mechanics*, Vol. 35, 2003, pp. 341-372.

[43] Shemdin, O.H. and Hsu, E.Y., "Direct measurement of aerodynamic pressure above a simple progressive gravity wave," *Journal of Fluid Mechanics*, Vol. 30, 1967, pp. 403-416.

[44] Sullivan, P.P., McWilliams, J.C., and Moeng, C.-H., "Simulation of turbulent flow over idealized water waves," *Journal of Fluid Mechanics*, Vol. 404, 2000, pp. 47-85.

[45] Sullivan, P.P., Edson, J.B., Hristov, T., and McWilliams, J.C., "Large eddy simulations and observations of atmospheric marine boundary layers above non-equilibrium surface waves," *Journal of the Atmospheric Sciences*, Vol. 65, 2008, pp. 1225-1245.

[46] Sussman, M., Smereka, P., and Osher, S., "A level set approach for computing solutions to incompressible two-phase flow," *Journal of Computational Physics*, Vol. 114, 1994, pp. 146-159.

[47] Sussman, M., Fatemi, E., Smereka, P., and Osher, S., "An improved level set method for incompressible two-phase flows," *Computers and Fluids*, Vol. 27, 1998, pp. 663-680.

[48] Sussman, M. and Puckett, E.G., "A coupled level set and volume-of-fluid method for computing 3d and axisymmetric incompressible two-phase flows," *Journal of Computational Physics*, Vol. 162, 2000, pp. 301-337.

[49] van Berlekom, W.B., "Wind forces on modern ship forms-effects on performance," *Transactions of the North East Coast Institute of Engineers and Shipbuilders*, Vol. 97, No. 4, 1981, pp. 123-134.

[50] van der Vorst, H.A., "Bi-CGSTAB: a fast and smoothly converging variant of Bi-CG for the solution of nonsymmetric linear systems," *SIAM Journal on Scientific and Statistical Computing*, Vol. 13, 1992, pp. 631-644.

[51] Vasilic-Melling, D., "Three-dimensional turbulent flow past rectangular bluff bodies," PhD Thesis, University of London, Imperial College, 1976.

[52] Werner, H. and Wengle, H., "Large-eddy simulation of turbulent flow over and around a cube in a plate channel," *Proceedings of the 8th Symposium on Turbulent Shear Flows*, Munich, Germany, 1991, pp. 155-168.

[53] Wills, J.A.B., "Recent research on wind loading," *Philosophical Transactions of the Royal Society A*, Vol. 334, 1991, pp. 229-240.

[54] Wnek, A.D. and Guedes Soares, C., "Charpter 15: Nnumerica analysis of the shadow effect of a LNG floating platform on an LNG carrier under wind conditions," *Sustainable Maritime Transportation and Exploitation of Sea Resources*, CRC Press, 117C122, 2011.

[55] Xiao, F., "Implementations of multi-fluid hydrodynamic simulations on distributed memory computer with a fully parallelizable preconditioned Bi-CGSTAB method," *Computer Physics Communications*, Vol. 137, 2001, pp. 274-285.

[56] Yakhot, A., Orszag, S.A., Yakhot, V., and Israeli, M., "Renormalization group formulation of large-eddy simulations," *Journal of Scientific Computing*, Vol. 4, No. 2, 1989, pp. 139-158.

[57] Yakhot, V. and Orszag, S.A., "Renormalization group analysis of turbulence. I. Basic theory," *Journal of Scientific Computing*, Vol. 1, No. 1, 1986, pp. 3-51.

[58] Yang, D. and Shen, L.,"Characteristics of coherent vortical structures in turbulent flows over progressive surface waves," *Physics of Fluids*, Vol. 21, 2009, 125106.

[59] Yang, D. and Shen, L., "Direct-simulation-based study of turbulent flow over various waving boundaries," *Journal of Fluid Mechanics*, Vol. 650, 2010, pp. 131-180.

[60] Yang, D. and Shen, L., "Simulation of viscous flows with undulatory boundaries. Part I: Basic solver," *Journal of Computational Physics*, Vol. 230, 2011, pp. 5488-5509.

[61] Yang, D. and Shen, L., "Simulation of viscous flows with undulatory boundaries. Part II: Coupling with other solvers for two-fluid computations," *Journal of Computational Physics*, Vol. 230, 2011, pp. 5510-5531.

[62] Yang, D., Meneveau, C., and Shen, L., "Dynamic modeling of sea-surface roughness for large-eddy simulation of wind over ocean wavefield," *Journal of Fluid Mechanics*, Vol. 726, 2013, pp. 62-99.

[63] Yang, D., Shen, L., and Meneveau, C., "An assessment of dynamic subgrid-scale sea-surface roughness model," *Flow, Turbulence and Combustion*, Vol. 91, 2013, pp. 541-563.

[64] Yang, J., Bhushan, S., Suh, J. S., Wang, Z., Koo, B., Sakamoto, N., Xing, T., and Stern, F., "Large-eddy simulation of ship flows with wall-layer models on Cartesian grids," *Proceedings of the 27th Symposium on Naval Hydrodynamics*, Seoul, South Korea, 2008, pp. 282-301.

[65] Yelland, M.J., Moat, B.I., Pascal, R.W., and Berry, D.I., "CFD model estimates of the airflow distortion over research ships and the impact on momentum flux measurements," *Journal of Atmospheric and Oceanic Technology*, Vol. 19, 2002, pp. 1477-1499.

[66] Zakharov, V.E., "Stability of periodic wave of finite amplitude on the surface of a deep fluid," *Journal of Applied Mechanics and Technical Physics*, Vol. 2, 1968, pp. 190-194.